Journal of
Marine Science and Engineering

Article

Effects of Quartz Precipitation on the Abundance and Preservation of Organic Matter Pores in Cambrian Marine Shale in South China

Sile Wei [1,*], Mingyi Hu [1], Sheng He [2], Yanbo Shu [3], Tian Dong [2], Qing He [2], Wei Yang [4] and Quansheng Cai [1]

1 School of Earth Sciences, Yangtze University, Wuhan 430100, China
2 Key Laboratory of Tectonics and Petroleum Resources, Ministry of Education, China University of Geosciences, Wuhan 430074, China; dongtian@cug.edu.cn (T.D.)
3 No. 8 Oil Recovery Plant of PetroChina Changqing Oilfield Company, Xi'An 710021, China; shuyanbo_cq@petrochina.com.cn
4 Guangzhou Marine Geology Survey, China Geological Survey, Ministry of Natural Resources, Guangzhou 510075, China
* Correspondence: weisile@outlook.com

Abstract: To evaluate the effects of quartz precipitation on the abundance and preservation of organic matter pores in marine shale reservoirs, the type of authigenic quartz and the source of silica, as well as the corresponding relation of the Lower Cambrian Shuijingtuo Formation shale in South China were investigated. Quartz in the Shuijingtuo shale occurs as four different types: detrital quartz, replacement of biosiliceous debris, euhedral quartz filled in interparticle pores, and microquartz dispersed in a clay matrix. Euhedral quartz (1–5 µm) and matrix-dispersed microquartz (100–400 nm) are found to be the dominant forms of authigenic quartz. The euhedral quartz accumulates along the interparticle pores, and the porous organic matter fills the interior of the space. Microquartz is mainly wrapped in porous organic matter. Two silica sources were revealed: biogenic silica and clay-derived silica. Biogenic Si is most likely the major source for authigenic quartz in the organic-rich (total organic carbon (TOC) > 2.55 wt.%) samples, which accounts for 23–57 wt.% (average 35 wt.%) of the total Si. Based on petrographic observations, we posit that the precipitation of large-sized euhedral quartz in the interparticle pores most likely originated from biogenic silica in the early stage of diagenesis and that the silica for the clay matrix-dispersed microquartz is provided by biogenic silica and clay-derived silica. The observation of SEM images indicates that the precipitation of early diagenetic euhedral quartz in the interparticle pores enhances rock stiffness, and the buttressing effect can protect the organic matter pores from compaction during the late-stage burial diagenesis. In contrast, the precipitation of late diagenetic microquartz in the clay matrix can lead to a reduction in the capacity of the accommodation space to host retained petroleum, consequently leading to a reduction in the development of organic matter pores and the generation of shale gas.

Keywords: authigenic quartz; silica source; organic matter pores; pore development; marine shale

check for updates

Citation: Wei, S.; Hu, M.; He, S.; Shu, Y.; Dong, T.; He, Q.; Yang, W.; Cai, Q. Effects of Quartz Precipitation on the Abundance and Preservation of Organic Matter Pores in Cambrian Marine Shale in South China. *J. Mar. Sci. Eng.* **2023**, *11*, 1267. https://doi.org/10.3390/jmse11071267

Academic Editor: Assimina Antonarakou

Received: 18 May 2023
Revised: 4 June 2023
Accepted: 5 June 2023
Published: 21 June 2023

1. Introduction

As an unconventional energy source with huge resource potential, shale gas, which is characterized as self-generating and self-preserving, has been stimulating great exploration in many countries, including America, Canada, China, and others [1]. An organic matter pore, one of the significant pore types in shale reservoirs, serves not only as the primary storage space of adsorbed and free gas, but also as an important micro seepage channel for shale gas [2–4]. Therefore, the abundance and preservation of organic matter pores are of great significance for shale gas exploration and development [2,5–7].

The thermal simulation experiments of sealed gold-tube pyrolysis on shale rocks showed that the generation of a large number of organic matter pores and shale gas is mostly related to the thermal cracking of retained petroleum [8,9]. The higher the amount of retained petroleum or the lower the hydrocarbon expulsion efficiency in shale reservoirs, the more abundantly organic matter pores develop, leading to enrichment of shale gas [10]. For the research of conventional sand reservoirs, petroleum geologists focus on hydrocarbon expulsion efficiency and have carried out significant in-depth research on the controlling factors, such as the organic matter attributes (type, abundance, and thermal maturity), combination structures between the source rock and reservoir rock, and roof/floor sealing conditions of the source rock [7,8,10–13]. However, for unconventional shale reservoirs, the amount of retained petroleum is more significant and plays an important role in shale gas enrichment [8,12]. In addition to the factors that affect the efficiency of hydrocarbon expulsion mentioned above, the changes in pore space before and during the hydrocarbon expulsion period also have an important control effect on the amount of retained petroleum.

Precipitation of authigenic quartz in the shale reservoirs is suggested to rank second to mechanical compaction in affecting the pore space for retained petroleum [14–16]. Nevertheless, research has found that the rigid lattice formed by the self-generated embrittlement of siliceous cement has a strong resistance to compaction [14,17]. Therefore, although siliceous cement occupies some of the primary pores, it holds residual pores, providing favorable space for the migration and filling of residual oil during the oil generation period, and also has a protective effect on the organic matter pores generated by the later thermal cracking of residual oil. However, the siliceous cement observed in shale, especially marine shale, can be of various types and originates from multiple silica sources that formed during different diagenetic periods [18–20]. The complexity of the relationship between the quartz type and the siliceous source brings uncertainties to the assessments of the impacts of siliceous cement on the abundance and preservation of organic matter pores. Therefore, it is necessary to investigate the corresponding relationship between quartz types and silica sources.

The Lower Cambrian Shuijingtuo Formation marine shale in southern China has been recognized as another interval with a tremendous gas exploration potential, after the Upper Ordovician–Lower Silurian Wufeng–Longmaxi Formations shale [21–23]. In this study, a set of marine shale samples collected from the Shuijingtuo shale in the Yichang slope in southern China was investigated to determine the quartz types and silica sources, as well as the corresponding relation between them. More importantly, this study aims to gain insight into the impact of quartz precipitation on the abundance and preservation of organic matter pores.

2. Geological Setting

The Yichang slope zone is located south of the Huangling anticline, the middle of the Yangtze Craton, and is bordered by the Qinling–Dabie orogenic belt to the north and the Xuefeng orogenic belt to the south [24–26] (Figure 1). During the Sinian (Ediacaran) and Cambrian periods, the tectonic movement and sedimentary environment changed drastically in southern China. At the end of the Ediacaran period, the Tongwan orogenic movement formed an alternating structural unit of uplift and depression in the study area [27]. In terms of the sedimentary environment, the transgression from south to north in the Early Cambrian period ended the carbonate deposition of the Late Sinian Dengying Formation and started the deposition of black organic-rich shale in the Early Cambrian Shuijingtuo Formation. The paleogeographical background of uplift and depression restricted the distribution of Early Cambrian sedimentary facies and controlled the thickness of the shale in the Shuijingtuo Formation [22]. The eastern uplift area included shallow-water platform facies with thin shale, and the shale thickness in the local areas was <3 m, similar to that of the YD 3 well (Figure 1). Furthermore, the western depression area mainly belonged to the deep shelf facies, where the shale is thick, such as the 140 m thick shale in the EYY1 well (Figure 1). Overall, the Shuijingtuo shale in the Yichang slope is thick in the west and thin in the east. The lithology column shows that the lower part of the Shuijingtuo shale is dominated by black siliceous organic-rich shale, the middle part is mainly composed of dark gray clay-rich siliceous and calcareous shale, and the upper part mainly consists of gray limestone and dolomite (Figure 1).

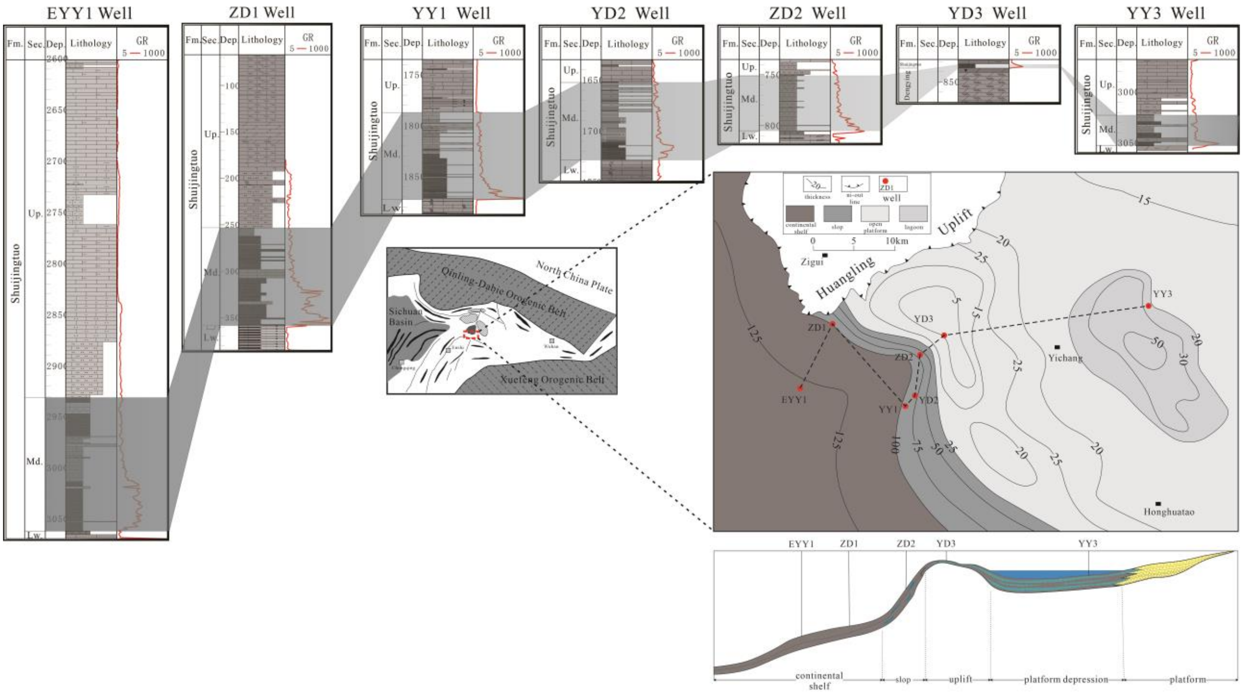

Figure 1. Geological map of the study area and lithology histograms of the Shuijingtuo Formation.

3. Methods

Twenty-nine shale samples were collected from the Shuijingtuo Formation of the EYY1 well in the Yichang slope zone, southern China. All the samples were analyzed for their TOC (total organic carbon), mineral composition, and major elements. Seven shale samples were selected for petrographic observation, including thin section observation, field-emission scanning electron microscopy (FESEM), SEM-based energy dispersive spectroscopy (EDS), and SEM-based cathodoluminescence (CL). The seven samples used for SEM petrographic observations were selected based on their TOC content and mineral compositions, which can essentially cover the overall Shuijingtuo Formation shales.

The TOC content was measured using an Elementar rapid CS cube. The analytical procedure consisted of removing carbonate with 7% HCl, drying at 80 °C for 10 h, and burning with 99.99% oxygen (O2) at 930 °C.

The bulk mineral composition was determined using XRD with an X'Pert PRO diffractometer (Malvern Panalytical B.V., Almelo, The Netherlands). The working voltage, current, radiation, and scanning speed were 40-kV, 40 mA, Cu Kα (λ = 0.15416 nm), and 0.417782° (2θ)/s, respectively, in a continuous mode with a step size of 0.017° in the range of 3–65°. The clay fraction mineralogy was reported by Wei et al. [28].

The major elements, including Si, Al, Fe, Mn, Ti, and Cr, were analyzed using an X-ray fluorescence spectrometer (XRF) (Zsx Primus II, Rigaku, Tokyo, Japan) in Wuhan SampleSolution Analytical Technology Co., Ltd. Powdered samples were dried in an oven for 12 h to remove free and adsorbed water and then heated to determine the loss on ignition. The X-ray tube was a 4.0 kW end window Rh target, and the test conditions comprised a voltage of 50 kV and a current of 60 mA. All the major elemental analysis lines were kα. The data were corrected using the theoretical α coefficient method. The relative standard deviation was <2%.

Thin sections of the shale samples were examined using conventional transmitted polarized light microscopy (Leica DM4500P, Tokyo, Japan). Before SEM imaging, the shale sample was first mechanically cut and the side perpendicular to the bedding plane was polished using Ar ion-beam milling (Leica EM TIC 3X). Subsequently, the samples were inspected using a ZEISS GeminiSEM FESEM instrument coupled with EDS and a cathodoluminescence (CL) detector. SEM imaging, EDS mapping, and CL imaging were performed at an accelerating voltage of 5–10 kV and a working distance of ~5–10 mm.

4. Results

4.1. Bulk Rock Properties

The results of the XRD analysis are depicted in Table 1. The Shuijingtuo shale is dominated by quartz and clay minerals. The quartz content ranges from 14 to 75 wt.%, averaging 53 wt.%. The content of clay minerals ranges from 9 to 53 wt.%, with an average of 20 wt.%. The XRD analysis of the fine powders (<2 μm) shows that the clay minerals are dominated by illite (56–90 wt.%, average 78 wt.%), followed by a mixed layer of illite/smectite (I-S) (10–44 wt.%, average 22 wt.%) [28].

Table 1. Depth, TOC content, mineral compositions, and concentrations of major elements of the Shuijingtuo shale samples.

Depth (m)	Organic	TOC (%)	Quartz (wt.%)	Carbonate (wt.%)	Clay (wt.%)	SiO_2 (wt.%)	Al_2O_3 (wt.%)	Fe_2O_3 (wt.%)	MnO (wt.%)	Zr (ppm)	Al/(Al + Fe + Mn)
2939.08	-lean	1.38	24	16	53	45.21	10.36	3.40	0.03	118	0.70
2975.53	-lean	1.63	28	33	30	31.47	6.21	3.45	0.06	55.6	0.57
2978.08	-lean	1.58	20	44	25	29.35	7.73	4.76	0.07	73.5	0.55
2983.63	-lean	2.47	47	8	30	59.62	12.81	3.32	0.02	122	0.74
2984.98	-lean	2.21	48	8	31	60.80	12.21	3.25	0.02	114	0.74
2989.32	-lean	1.80	34	31	26	40.68	7.00	3.90	0.05	65	0.57
2996.32	-lean	2.27	45	5	34	60.44	13.02	4.85	0.05	119	0.67
3003.50	-rich	2.72	64	5	20	68.67	9.49	2.10	0.02	85.1	0.77
3004.88	-rich	3.08	69	9	12	68.48	7.21	2.27	0.02	60.9	0.70
3007.34	-rich	2.93	58	5	24	65.38	10.71	3.91	0.02	92.9	0.67
3007.75	-rich	3.02	59	5	22	65.46	10.42	2.80	0.03	90.6	0.74
3008.78	-rich	3.47	59	8	21	63.06	9.45	2.75	0.03	83.8	0.72
3011.50	-rich	4.66	62	4	17	65.53	10.11	2.62	0.02	99.3	0.74
3020.54	-rich	4.33	57	8	17	62.42	9.20	3.77	0.02	131	0.65
3023.83	-rich	5.22	62	6	11	63.76	9.40	3.63	0.03	127	0.66
3024.33	-rich	5.24	57	7	20	62.71	9.27	3.55	0.02	123	0.66
3026.38	-rich	6.20	61	8	13	62.86	8.84	2.83	0.03	108	0.70
3030.18	-rich	5.78	60	8	12	62.26	8.68	3.25	0.03	110	0.67
3034.92	-rich	5.76	63	6	18	66.27	8.09	3.00	0.02	98.1	0.67
3037.53	-rich	4.76	55	13	16	57.55	8.54	3.67	0.03	100	0.64
3041.33	-rich	5.88	65	4	18	64.59	7.64	5.96	0.02	93.0	0.49
3043.48	-rich	5.08	63	4	20	69.82	7.22	2.44	0.01	85.8	0.69
3044.76	-rich	6.06	75	5	11	72.98	5.97	2.21	0.01	74.6	0.67
3053.03	-lean	2.54	22	61	11	24.29	3.70	1.58	0.02	48.8	0.64
3053.28	-rich	7.73	68	7	9	65.61	8.13	3.79	0.01	103	0.62
3053.88	-rich	8.25	72	5	10	68.04	6.58	2.96	0.01	83.0	0.63
3054.20	-rich	7.55	56	5	18	64.78	8.57	3.69	0.02	113	0.64
3062.70	-lean	2.34	14	60	16	37.73	8.18	2.77	0.02	112	0.69
3064.45	-lean	2.37	28	42	17	39.67	7.08	2.44	0.01	88.9	0.69

The TOC content of the Shuijingtuo shale varies between 1.38 and 8.25 wt.% (average 4.05 wt.%) (Table 1). The TOC content shows a positive correlation with the quartz content, but exhibits two distinct slopes (Figure 2), implying a difference in the silica source between them. Based on the slope, the samples with TOC < 2.55 wt.% are classified as organic-lean shale, and those with a TOC > 2.55 wt.% are classified as organic-rich shale.

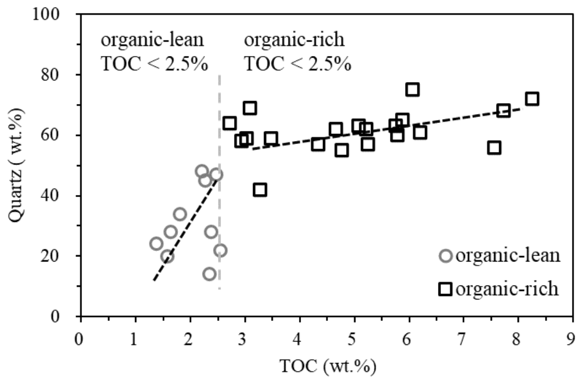

Figure 2. Relationship between TOC and bulk quartz (XRD) content. The organic-lean (TOC < 2.55 wt.%) and organic-rich (TOC > 2.55 wt.%) samples exhibit two distinct positive slopes, implying a difference in silica source between them.

4.2. Quartz Types and Silica Sources

4.2.1. Quartz Types

Compared to sandstone, identifying quartz types in shale reservoirs is more difficult because of the small particle size of the mineral. The widely utilized high-resolution FESEM combined with energy dispersive X-ray (SEM-EDS) and cathodoluminescence (SEM-CL) is a new technique that can differentiate authigenic quartz from detrital quartz at a submicrometer scale, and can identify quartz types based on the information gained from SEM images on crystal shape, spatial distribution, and CL response [29].

Based on the thin section and SEM observations, four quartz types were identified in the Shuijingtuo shale: detrital quartz, replacement of biosiliceous debris, euhedral quartz filling the interparticle pores, and microquartz dispersed in the clay matrix.

Detrital quartz is subangular to angular in shape and ~5–20 µm in size and can be easily identified from the bright CL intensity (Figure 3).

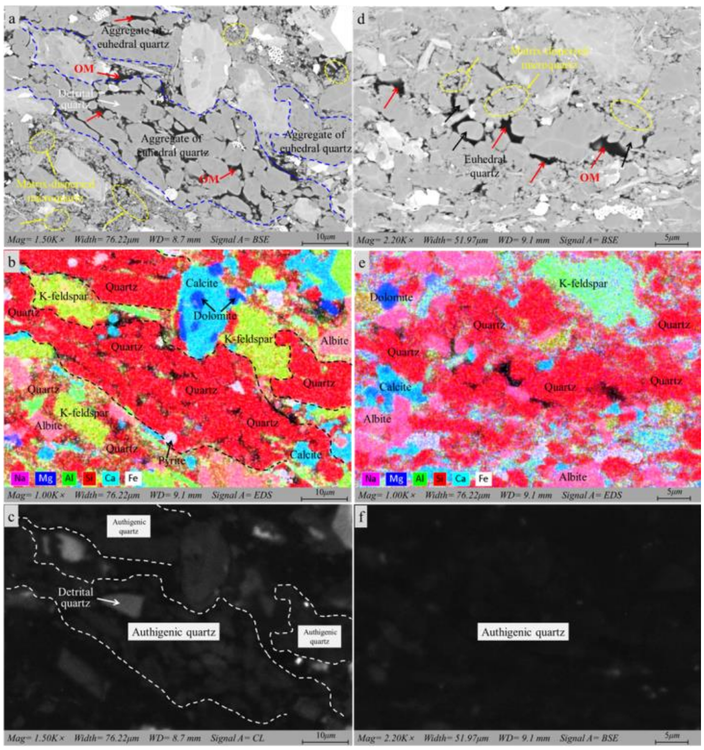

Figure 3. SEM, SEM-CL, and SEM-EDS images showing the petrographic features of authigenic and detrital quartz. (**a**) SEM image from sample 3026.38 m showing that the authigenic euhedral quartz

occurs as aggregates filled in the interparticle pores and the microquartz is dispersed in the claymineral matrix. The euhedral quartz is much larger than the microquartz. (**b**) SEM-EDS images confirming mineral identification, the same area as (**a**). (**c**) SEM-CL images (same area as (**a**)) showing the authigenic quartz has a dark, homogeneous luminescence and detrital quartz has a bright CL intensity. (**d**) SEM image from sample 3007.75 m showing that the authigenic euhedral quartz occurs occasionally as discrete grains. (**e**) SEM-EDS images confirming mineral identification, the same area as (**d**). (**f**) SEM-CL image (same area as (**a**)) showing the authigenic quartz with non-luminescence. Yellow arrows and boxes in (a) represent matrix-dispersed microquartz; red arrows in (**a**,**d**) represent organic matter (OM); blue dashed boxes in (**a**) represent aggregate of euhedral quartz; black arrows in (**d**) represent single euhedral quartz particle.

Radiolarians and sponge spicules are siliceous organisms that are commonly developed in the Lower Cambrian Shale in southern China [30,31], and these organisms were also observed abundantly in this study. As illustrated in Figure 4, siliceous organisms are more abundant in the organic-rich samples than in the organic-lean samples. The biosiliceous debris is poorly preserved and extensively replaced and filled by authigenic minerals. The most abundant replacement and filling of biosiliceous debris are carbonate minerals and pyrite (Figure 5).

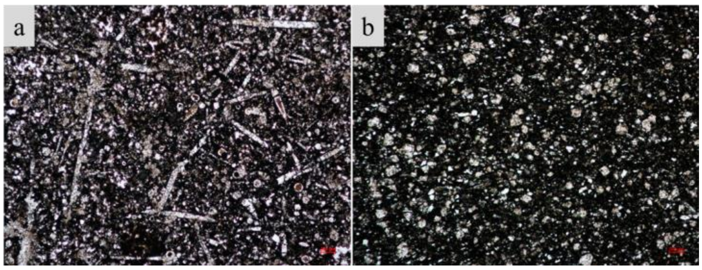

Figure 4. Thin-section images showing difference in the abundance of biosiliceous debris between organic-rich and organ-lean samples. (**a**) Organic-rich sample from 3011.50 m (TOC = 4.66 wt.%) presenting abundant radiolarians and sponge spicules. (**b**) Organic-lean sample from 3064.45 m (TOC = 2.37 wt.%) with essentially nil in the siliceous organism.

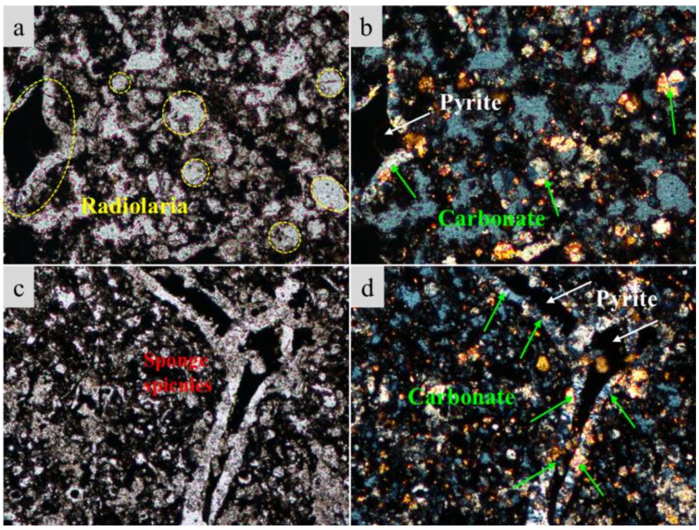

Figure 5. Example showing the replacement and filling of radiolarians and sponge spicules, sample depth = 3011.50 m. The biosiliceous debris is extensively replaced and filled by the carbonate minerals (green arrows) and pyrite (white arrows). Images of (**a**,**c**) were observed with the plane-polarized light. Images of (**b**,**d**) were observed with cross-polarized light. (**a**,**b**) are the same area; (**c**,**d**) are the same area.

Euhedral quartz filling the interparticle pores (Figures 6 and 7) and microquartz dispersed in the clay matrix (Figure 8) are found to be the predominant authigenic quartz types in the Shuijingtuo shale. Both have a dark and homogeneous CL intensity (Figure 3). Clay matrix-dispersed microquartz is a common quartz type that was reported in many other mudrocks [18–20]. Euhedral quartz filling the interparticle pores is a particular quartz type that is rarely reported in shales, except for those from the marine shales in southern China, such as Shuijingtuo shale and Wufeng–Longmaxi shale [17,28]. Euhedral quartz can be easily distinguished from clay matrix-dispersed microquartz by the following three petrographic features. Euhedral quartz occurs commonly as aggregates composed of several macrocrystalline quartz crystals or occasionally as discrete grains. The SEM image statistics from six estimated shale samples show that the size of the macrocrystalline quartz crystals is 1–5 μm (average 3 μm) (Figure 9a). In contrast, matrix-dispersed microquartz is much smaller, primarily 100–400 nm (average 200 nm) (Figure 9b). Different from the euhedral quartz, microquartz typically coexists with clay minerals (Figures 6–8).

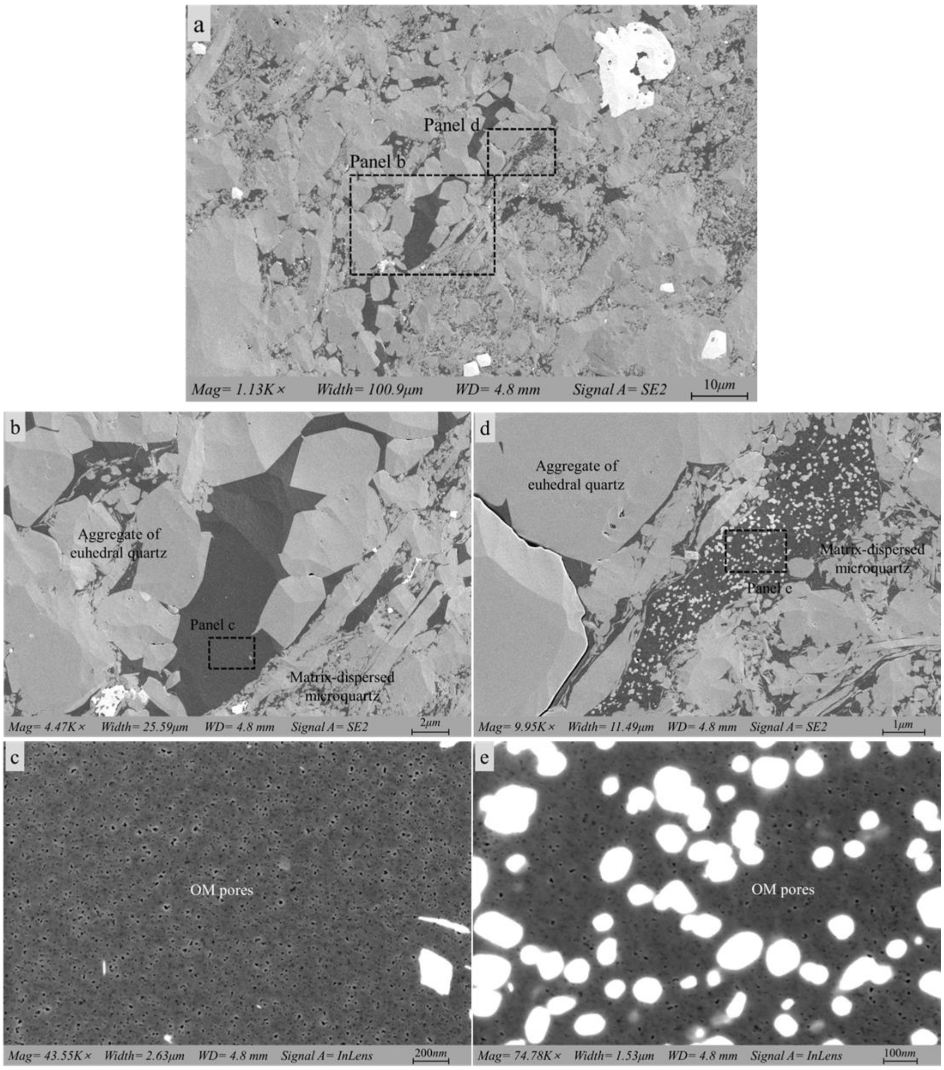

Figure 6. Images showing the euhedral quartz filling the interparticle pores and microquartz dispersed in clay matrix, sample depth = 3026.38 m. (**a**) Abundant euhedral quartz and microquartz dispersed in shale reservoir. (**b**) Enlargement of image (**a**). The euhedral quartz linings along the interparticle pores and the porous organic matter fills the interior of the space. (**c**) Enlargement of image (**b**). Interparticle pore-filled organic matter develops pores with rounded to sub-rounded shape. (**d**) Enlargement of image (**a**). Microquartz dispersed in clay matrix. (**e**) Enlargement of image (**d**) showing abundant organic matter pores.

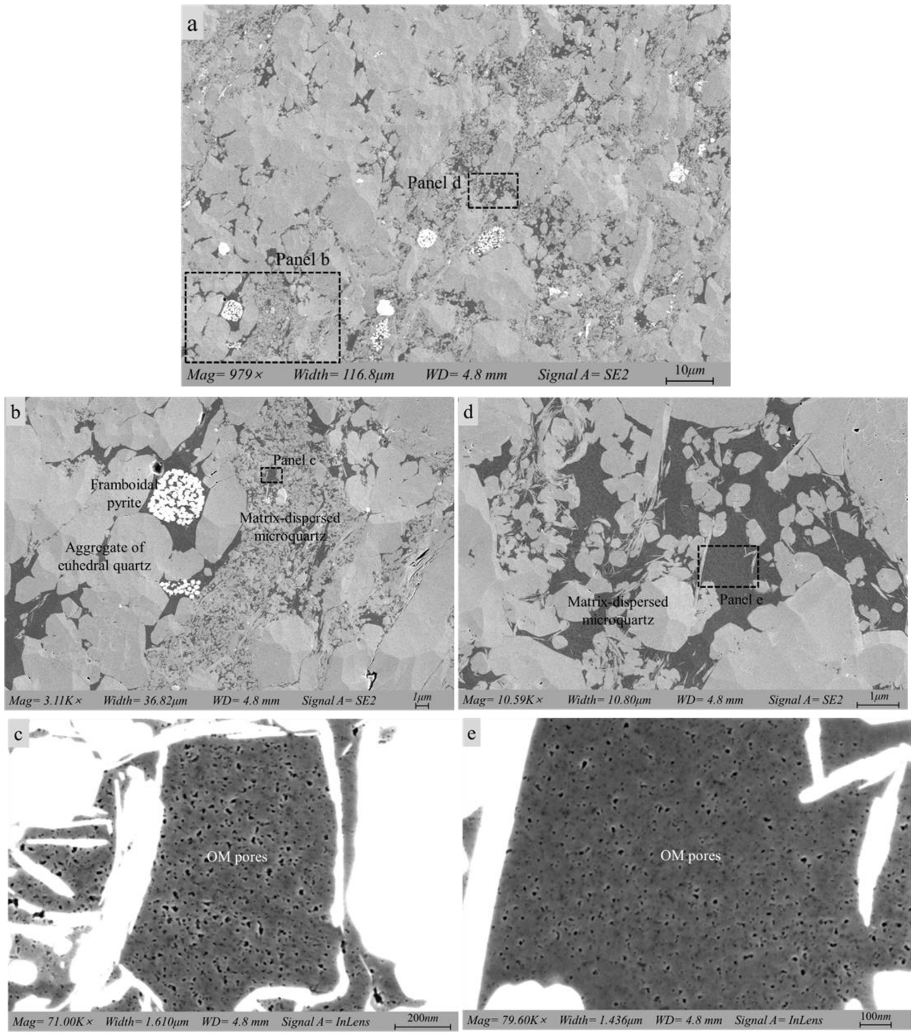

Figure 7. (**a**) SEM images showing the spatial distribution of euhedral quartz and microquartz, sample depth = 3026.38 m. (**b**,**d**) Enlargement of image (**a**) showing that microquartz coexists with the porous organic matter in the clay mineral matrix. (**c**) Enlargement of image (**b**) showing organic matter pores. (**e**) Enlargement of image (**d**) showing organic matter pores.

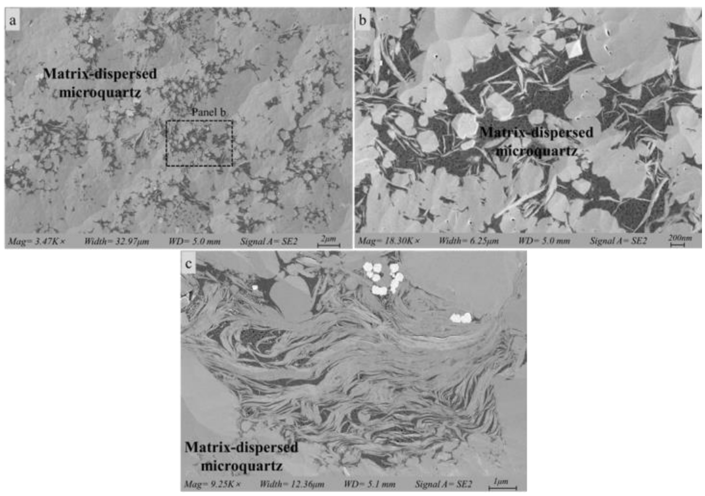

Figure 8. This SEM images showing the microquartz dispersed in clay mineral matrix and is mostly wrapped by the porous organic matter. (**a**) Sample depth = 3041.33 m. (**b**) Enlargement of image (**a**). (**c**) Sample depth = 2996.32 m.

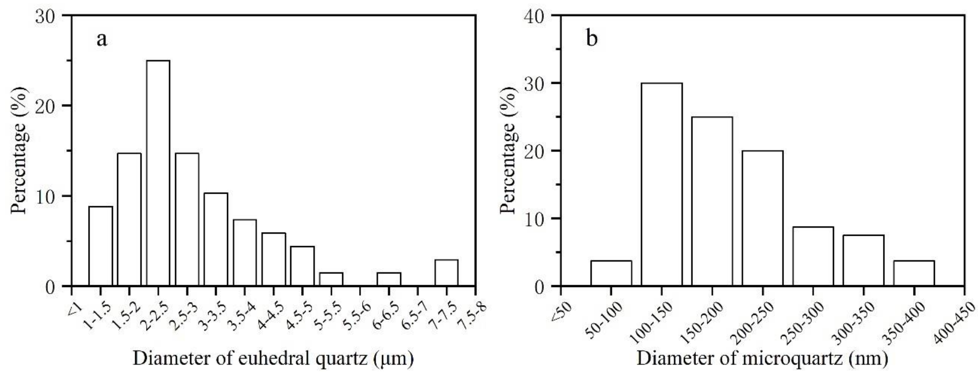

Figure 9. Histogram of diameter of euhedral quartz (**a**) and microquartz (**b**). The size of macrocrystalline quartz crystals is in the range of 1–5 μm (average 3 μm). Matrix-dispersed microquartz is much smaller, mostly between 100 nm and 400 nm (average 200 μm).

The SEM images show that the authigenic quartz typically coexists with porous organic matter in the pore space (Figures 6–8). However, the two types of authigenic quartz have different positional relationships with porous organic matter. In the interparticle pores, the euhedral quartz is observed to be arranged around the pores and the porous organic matter fills the interior of the space composed of euhedral quartz. Conversely, in the clay matrix pores, microquartz is mostly wrapped by porous organic matter.

4.2.2. Silica Sources

Previous studies have suggested that common silica sources include the dissolution of siliceous skeletons (biogenic silica), transition of smectite to illite (clay-derived silica), pressure dissolution of detrital quartz, alteration of feldspar, alteration of volcanic ash, and precipitation of submarine hydrothermal venting [32–34].

Volcanic ash is highly unstable and will dissolve rapidly to release a variety of cations that form bentonite composed of quartz, zircon, apatite, kaolinite, chlorite, zeolite, etc. [35]. In the study area, no volcanic ash layer has been identified in the Shuijingtuo Formation and there are no associated reports about a volcanic eruption during the Early Cambrian period. Furthermore, the mineral compositions detected by XRD analysis reveal that no volcanic ash alteration occurs in the Shuijingtuo shale. Thus, the possibility of volcanic ash being the silica source for authigenic quartz can be excluded. Few intergranular contacts between detrital quartz are observed in the SEM images; therefore, pressure dissolution is less likely to be a silica source. Similarly, no specific petrographic evidence supports feldspar alteration as a potential silica source.

The geochemical proxies (e.g., Al, Fe, Mn, Ti) are effective methods for discriminating the hydrothermal origin from the nonhydrothermal origin of silica [19,20]. The compositions of hydrothermal sedimentary rocks are usually characterized by high Fe and Mn. In contrast, nonhydrothermal sedimentary rocks are enriched in Al and Ti [36]. The ratio of Al/(Al + Fe + Mn), ternary diagram of Al–Fe–Mn, and plot of Fe/Ti–Al/(Al + Fe + Mn) are used to determine the silica input of the hydrothermal source [37,38]. Rocks with a pure hydrothermal origin of silica have a low value of Al/(Al + Fe + Mn) (<0.01), whereas Al/(Al + Fe + Mn) in rocks with pure biogenic silica is >0.60 [39]. The ratio of Al/(Al + Fe + Mn) in the Shuijingtuo shale is 0.49–0.77, with an average value of 0.66 (Table 1), indicating that there is no hydrothermal activity in the study area. Moreover, as illustrated in the Al–Fe–Mn ternary diagram, all the Shuijingtuo samples are plotted in the nonhydrothermal region, which is characterized by enrichment in Al relative to Fe and Mn (Figure 10). Therefore, according to the data for Al, Fe, and Mn, it can be concluded that the Shuijingtuo shale in the study area is related to nonhydrothermal deposition and there is no silica input from the hydrothermal source.

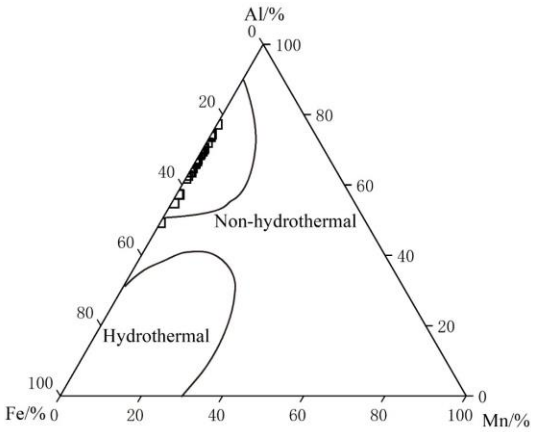

Figure 10. Ternary diagram of Al–Fe–Mn determining the silica input of the hydrothermal and non-hydrothermal source. The examined Shuijingtuo shale samples are plotted in the nonhydrothermal region, indicating that there is no silica input of hydrothermal source of the Shuijingtuo shale in the study area.

The maturity of the examined Shuijingtuo shale is in the stage of dry gas (~1.93–2.20% Ro, [28]), which means that the shale has mostly experienced sufficient temperature to induce substantial illitization of smectite [40]. The clay minerals of the Shuijingtuo shale are mainly composed of illite (78 wt.%, average), followed by a mixed layer of I-S (22 wt.%) [28]. The high ratio of illite to clay minerals implies that the Shuijingtuo shale has possibly completed the conversion from smectite to illite, during which a certain amount of silica was released [41]. Therefore, the transition of smectite to illite is one of the potential sources of silica.

This study suggests the dissolution of siliceous skeletons is the silica source for the authigenic quartz precipitation in the organic-rich samples. The initial silica phase of siliceous skeletons is unstable opal-A, which can quickly transit to metastable opal-CT and ultimately to the stable end product quartz [42,43]. The thin-section images show that many radiolarian and sponge spicules are observed in the organic-rich shales, but are almost absent in organic-lean shales (Figure 4). The substantial replacement of radiolarian and sponge spicules observed within the organic-rich shale samples (Figure 5) confirms that the biosiliceous debris has experienced dissolution and has supplied massive silica for quartz precipitation.

The plot of zirconium (Zr) versus Si is another method that is utilized to examine the biogenic silica source [44–46]. Zr is typically associated with heavy mineral zircon that existed in the detrital fraction and is interpreted to be a proxy for a detrital source of silica [44–46]. A positive correlation between Zr and Si is interpreted to indicate a detrital source for silica, such as in the Jurassic Haynesville-Bossier shale [47], whereas a negative correlation is used to indicate the input of biogenic silica, such as in the Devonian Muskwa shale [45]. In this study, two opposite Zr–Si trend lines were obtained among the Shuijingtuo samples (Figure 11a). Similar results have been reported in the Devonian Horn River Group shale [46] and the Muskwa Formation shale [45]. Coincidentally, the samples in which Zr increases with an increase in Si (detrital trend line) (Figure 11a) are all the organic-lean shales that have a high slope in the TOC–quartz plot (Figure 2). Correspondingly, the samples that lie on the biogenic trend line (Figure 11a) are all the organic-rich shales, which have a low slope in the TOC–quartz plot (Figure 2). Therefore, we infer that the source of silica in the organic-lean samples is major detrital silica, and biogenic silica accounts for at least a certain proportion in the organic-rich samples. The analyses of the silica source in organic-lean and organic-rich shales by Zr–Si plot coincide with the petrographic observations, that is, organic-rich samples are rich in siliceous skeletons, whereas organic-lean samples are essentially nil (Figure 4). The content of biogenic silica will be discussed in the following section.

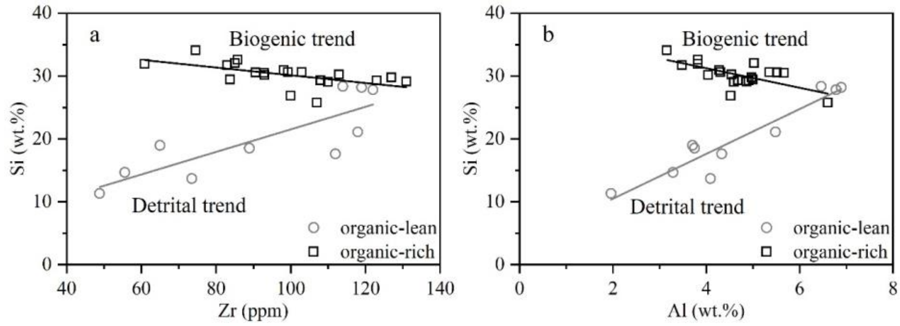

Figure 11. Relationships between Si and Zr (**a**) and Al (**b**) concentration in the Shuijingtuo Shale samples from XRF datasets. The positive lines are termed the "detrital trend", indicating a detrital source for silica. The negative lines are termed the "biogenic trend", indicating the input of biogenic silica. Samples in which Zr and Al increase with the increase of Si are all the organic-lean shales that have a high slope in the TOC–quartz plot (Figure 2). Samples that lie on the biogenic trend line are all the organic-rich shales, which have a low slope in the TOC–quartz plot (Figure 2).

4.3. Content of Biogenic Silica

Excess Si, as proposed by Sholkovitz and Price [48], is defined as the content that exceeds the Si concentration in the terrigenous components (normal detrital background). Excess Si is widely adopted to quantify the degree of enrichment of non-terrigenous silica [49]. Excess (or non-terrigenous) Si is defined as the sum of the biogenic, hydrothermal, volcanic ash alteration silica, and other non-terrigenous input Si [46,50]. Combined with the analyses of silica sources above, the excess Si in the Shuijingtuo shale refers to the biogenic Si content.

Excess Si is calculated as (total Si—detrital Si), which is generally estimated using the following formula: $Si_{excess} = Si_{sample} - [(Si/Al)_{background} \times Al_{sample}]$ [48]. The value of $(Si/Al)_{background}$ is important for excess Si estimation. However, we found that this value varies across different studies. The majority of studies typically use 3.11 as the value of $(Si/Al)_{background}$ [17,20,49,51,52], which is the average of 277 samples from the post-Archaean average shale, also called standard shale [53]. Some studies use the value 2.50 [54], which is the average Si/Al value of samples from the Amazon estuary zone of terrigenous material [48]. The lowest Si/Al value in the estimated samples was designated as the background value [55]. Therefore, the value of $(Si/Al)_{background}$ remains controversial and differs among different studies. Van der Weijden [56] and Tribovillard et al. [57] hold that the composition of the commonly used standard shale and the reference values of normalized elements are not necessarily representative of the local or regional sediments in the study area.

Figure 11b shows the Al–Si plot. Similar to the Zr–Si plot, the organic-lean samples lie on the detrital (positive) trend line, and the organic-rich shales lie on the biogenic (negative) trend line (Figure 11). As analyzed above, silica in organic-lean samples is the major detrital in origin. Therefore, the organic-lean samples can be regarded as normal detrital shales in the EYY1 well. Moreover, samples above the detrital trend line have a higher Si content, which is sourced from the dissolution of siliceous skeletons (radiolarian and sponge spicules). Based on the definition of the excess Si, the excess (biogenic) Si is calculated as the absolute difference between Si measured in a sample and the Si versus Al regression line (detrital trend line) for the organic-lean samples. The determined biogenic Si is shown in Table 2. The results show that the biogenic Si in the organic-rich shales is 7–19 wt.% (average 11 wt.%), and the ratio of biogenic Si to total Si is 23–57 wt.% (average 35 wt.%) (Table 2). If the biogenic Si precipitates in the form of quartz, ~15–42 wt.% biogenic quartz will be formed, accounting for 26–55 wt.% of the total quartz (XRD). Compared to the proportion of clay-derived quartz (discussed below), biogenic silica is the major source of the authigenic quartz in the organic-rich shales. Biogenic silica as the primary source has also been reported in other marine shales, such as the Upper Cretaceous Eagle Ford shale in southern Texas [18], Upper Pennsylvanian Cline shale in the Midland basin [14], Mississippian Bowland shale in the Craven basin [54], and Upper Ordovician Wufeng–Lower Silurian Longmaxi shale in the Sichuan basin [51].

Table 2. Results of the calculated biogenic Si and biogenic quartz of the Shuijingtuo shale samples.

Sample ID	Depth (m)	Organic	TOC (wt.%)	Quartz (XRD wt.%)	Biogenic Si (wt.%)	Biogenic Si /Total Si	Biogenic Quartz (wt.%)	Biogenic Quartz /Quartz (XRD)
EYY24	2939.08	-lean	1.38	24	-	-	-	-
EYY42	2975.53	-lean	1.63	28	-	-	-	-
EYY47	2978.08	-lean	1.58	20	-	-	-	-
EYY61	2983.63	-lean	2.47	47	-	-	-	-
EYY64	2984.98	-lean	2.21	48	-	-	-	-
EYY74	2989.32	-lean	1.80	34	-	-	-	-
EYY90	2996.32	-lean	2.27	45	-	-	-	-
EYY103	3003.50	-rich	2.72	64	10.77	34%	23	36%
EYY106	3004.88	-rich	3.08	69	14.98	47%	32	47%
EYY111	3007.34	-rich	2.93	58	6.92	23%	15	26%
EYY112	3007.75	-rich	3.02	59	7.51	25%	16	27%
EYY114	3008.78	-rich	3.47	59	8.22	28%	18	30%
EYY119	3011.50	-rich	4.66	62	8.12	27%	17	28%
EYY138	3020.54	-rich	4.33	57	8.39	29%	18	32%
EYY147	3023.83	-rich	5.22	62	8.65	29%	19	30%
EYY148	3024.33	-rich	5.24	57	8.40	29%	18	32%
EYY152	3026.38	-rich	6.20	61	9.28	32%	20	33%
EYY159	3030.18	-rich	5.78	60	9.30	32%	20	33%
EYY167	3034.92	-rich	5.76	63	12.29	40%	26	42%
EYY172	3037.53	-rich	4.76	55	7.36	27%	16	29%
EYY180	3041.33	-rich	5.88	65	12.35	41%	26	41%
EYY187	3043.48	-rich	5.08	63	15.58	48%	33	53%
EYY190	3044.76	-rich	6.06	75	19.41	57%	42	55%
EYY204	3053.03	-lean	2.54	22	-	-	-	-
EYY205	3053.28	-rich	7.73	68	11.91	39%	26	38%
EYY206	3053.88	-rich	8.25	72	15.96	50%	34	48%
EYY207	3054.20	-rich	7.55	56	10.70	35%	23	41%
EYY223	3062.70	-lean	2.34	14	-			-
EYY226	3064.45	-lean	2.37	28	-			-

5. Discussions

5.1. Corresponding Relation between Quartz Types and Silica Sources

Two types of authigenic quartz grain are present in the Shuijingtuo shale: one is large-sized euhedral quartz (1–5 µm) filling the interparticle pores and the other is small-sized microquartz dispersed in the clay mineral matrix. The silica for the authigenic quartz is proved to be sourced from the dissolution of siliceous skeletons and the transformation of smectite to illite. These facts raise a question: What is the corresponding relationship between the quartz types and silica sources? Determining the answer to the question is of great significance for the assessment of the impacts of siliceous cement on the abundance and preservation of organic matter pores.

The SEM-CL cannot distinguish between the authigenic quartz formed in the early and late diagenetic stage because both have a dark, non-luminescent CL response. Previous studies have suggested that the dissolution of siliceous skeletons to form the end product quartz occurs at relatively low temperatures [32]. Iijima and Tada [35] reported that the temperature at which opal-A starts to change to opal-CT is within a range between 22 °C and 33 °C (550–1180 m) within Neogene siliceous sediments in northern Japan, and the transformation of opal-CT into quartz starts at a temperature of 28–44 °C (810–1240 m). The reaction of smectite illitization accompanied by silica release occurs at 60–100 °C [58–60].

The comparison of reaction temperature indicates that the precipitation of biogenic quartz is earlier than that of clay-derived quartz.

At shallow depths (lower temperature), the mudrocks have higher porosity (~10–55% at 1 km [61]), which means that there are sufficient primary pores with large pore size for the precipitation of biogenic quartz. Therefore, the large-sized euhedral quartz filling the interparticle pores most likely resulted from the dissolution of siliceous skeletons at an early stage of diagenesis. With an increase in the burial depth and temperature, the transformation of smectite to illite is triggered and the mechanical compaction strength also increases, which leads to a significant loss of porosity and a decrease in pore size. Hence, the quartz sourced from the illitization reaction theoretically has a small size, which was illustrated clearly by the experiments of clay mineral transformation [62,63]. However, we can only conclude that the observed small-sized microquartz is partially derived from the clay transformation because the volume of microquartz presented in the SEM images is much larger than that generated from the transformation of clay minerals, which is discussed below.

The reaction of the illitization of smectite is complex and the amount of released quartz is still disputed. Van de Kamp [64] suggested that, assuming Al conservation, the smectite illitization yields about 17–28 wt.% quartz as a proportion of the original smectite (about 25–41 vol.% of the final illite, the molar volume of clay fraction refers to Środoń et al. [65]). However, Milliken and Olson [15] documented that the illitization based on the Al balance seems untenable because this reaction leads to high volume loss (60%) in the clay fraction. Milliken [16] proposed a 1:1 (smectite:illite) molar balance reaction, which releases 0.47 mol silica without causing an immense volume loss of the clay fraction. If the released silica precipitated in its entirety, it would yield a volume of quartz equivalent to ~6 vol.% of the final clay minerals [16]. However, the observations in high-magnification SEM images differ from the reaction formulas. The point-count volume of the microquartz and clay minerals is listed in Table 3. The results show that the volume ratio of microquartz to clay mineral is 0.67–4.32, which is much higher than that of the aforementioned smectite to illite reactions. Notably, these ratio values do not represent the entire shale sample because there are not enough point-counted SEM images to equate the micro with the macro, which is a common issue for microscopic observations. Nevertheless, these results suggest that the content of microquartz is too high to be obtained fully from the clay mineral transformation. Therefore, the biogenic silica most likely provides mass silica for the microquartz precipitation, which is consistent with the views of Peng et al. [14] in the Cline shale and Milliken and Olson [15] in the Mowry shale. More specifically, the dissolution of siliceous skeletons and transformation of smectite to illite together provide the silica for the precipitation of clay matrix-dispersed microquartz.

Table 3. Point-count volume of clay mineral, microquartz, and organic matter in high-magnification SEM images.

Depth (m)	Organic	TOC (wt.%)	Clay Mineral (vol.%)	Microquartz (vol.%)	Organic Matter (vol.%)	Other Mineral (vol.%)
3053.03	-lean	2.54	41.08	27.5	18.69	12.73
3020.54	-rich	4.33	33.24	40.13	24.58	2.05
3041.33	-rich	5.88	16.67	52.20	31.13	-
3054.20	-rich	7.55	12.99	56.17	29.55	1.29

5.2. Effects on the Abundance and Preservation of Organic Matter Pores

As a significant pore type in the shale pore systems, organic matter pores could supply extensive pore spaces for storing adsorbed and free shale gas [2,27,66,67]. According to the origin, organic matter pores can be divided into primary and secondary (migrated) types [3,9,28]. The primary types are commonly found in kerogen in immature shales and are considered to be inherited from organic macerals [3,68,69]. Formation of the secondary type is stimulated by the evolution of the kerogen and secondary organic matter (solid bitumen or oil) during thermal maturation [28,70–72]. Compared to the primary type, the secondary type is more abundant and well-connected, which is advantageous for the storage and transport of shale gas [12]. Wei et al. [28] reported that most of the porous organic matter in the Shuijingtuo shale is migrated organic matter, which has thermally evolved from the initial liquid petroleum phase of solid bitumen or oil into pyrobitumen. The terms of kerogen, oil, solid bitumen, and pyrobitumen are derived from the work of Mastalerz et al. [73].

The thermal cracking of the retained petroleum was documented to be the main mechanism for the massive shale gas generation and formation of the organic matter pores by the modeling experiments of gas generation and pore evolution by the sealed gold-tube pyrolysis [8,9]. Therefore, the amount of retained petroleum is significantly related to shale gas enrichment and reservoir quality. In addition to well-known factors, such as organic matter attributes (type, abundance, and thermal maturity), combination structures between the source rock and reservoir rock, and roof/floor sealing conditions of the source rock, which are critical for evaluating the amount of retained petroleum, the changes in pore space before and during the hydrocarbon expulsion period have been found to be another important factor that controls the petroleum retention [8,10–12].

The relative time of authigenic quartz precipitation and liquid petroleum migration has an impact on the pore space. The presence of the porous organic matter embayed by euhedral quartz in the interparticle pores (Figures 6b and 7b) suggests that the migration of liquid petroleum occurred later than the precipitation of euhedral quartz. The observations agree with the analysis above that the euhedral quartz with a large grain size resulted from the dissolution of siliceous skeletons in the early diagenetic stage. The precipitation of the early diagenetic euhedral quartz can thus lead to a reduction in primary pores, as it occupies partial primary interparticle pores. It was suggested that the early diagenetic quartz could increase rock mechanical behavior to inhibit mechanical compaction [54,74]. In the primary interparticle pores, part of euhedral quartz exhibits a weak preferred orientation (Figures 3a and 6a), indicating that the quartz has undergone some mechanical compaction at a later stage. Due to the rigidity of the quartz framework, the primary pores retained some space for the subsequent migration of solid bitumen or oil. The rounded to sub-rounded organic matter pores (Figure 6c) indicate that the buttressing effect by the euhedral quartz framework can protect the organic matter pores from compaction during the late-stage burial diagenesis.

The presence of microquartz wrapped by the porous organic matter in the clay matrix pores (Figure 8) suggests a situation where the migration of liquid petroleum is coeval with or later than the precipitation of microquartz. If there is no microquartz precipitation in the clay matrix pores, there would be more pore space for the migration and retention of liquid petroleum, and more shale gas and organic matter pores would be generated.

6. Conclusions

1. In the estimated marine shale reservoir, quartz can be observed as four types, including detrital quartz, replacement of biosiliceous debris, euhedral quartz filled in the interparticle pores, and microquartz dispersed in a clay matrix.
2. The dominant forms of authigenic quartz are euhedral quartz and microquartz. Euhedral quartz is much larger (1–5 μm) than microquartz (100–400 nm). Moreover, they have different positional relationships with porous organic matter. The porous organic matter fills the interior of the space composed of euhedral quartz, whereas microquartz is mostly surrounded by porous organic matter.
3. The source of silica for the precipitation of authigenic quartz includes the dissolution of siliceous skeletons and the transition of smectite to illite. In the organic-rich shale samples, biogenic silica is most likely the major source for the authigenic quartz. The calculated excess Si (biogenic Si) ranges from 7 to 19 wt.% (average 11 wt.%), accounting for 23–57 wt.% (average 35 wt.%) of the total silica.

4. The large-sized euhedral quartz present in the interparticle pores most likely results from the dissolution of siliceous skeletons at an early diagenesis stage. The silica for the clay matrix-dispersed microquartz is jointly provided by biogenic silica and clay-derived silica.
5. The precipitation of early diagenetic euhedral quartz in the interparticle pores enhances rock stiffness, and the buttressing effect can protect the organic matter pores from compaction during the late-stage burial diagenesis. The precipitation of late diagenetic microquartz in the clay matrix can lead to a reduction in the retained petroleum, which would lead to a reduction in the amount of organic matter pores developed.

Author Contributions: Conceptualization, S.W., M.H., S.H., Y.S. and T.D.; methodology, S.W., M.H., S.H. and W.Y.; formal analysis, S.W., Q.H. and Q.C.; investigation, T.D., Q.H., W.Y. and Q.C.; resources, M.H., S.H. and T.D.; data curation, Y.S., Q.H. and W.Y.; writing—original draft preparation, S.W.; writing—review and editing, S.W., M.H., S.H., Y.S., T.D., Q.H., W.Y. and Q.C.; funding acquisition, S.W., S.H. and Q.C. All authors have read and agreed to the published version of the manuscript.

Funding: This research was funded by the Natural Science Foundation of Hubei Province (No. 2022CFB652) and the CNPC Innovation Fund (No. 2021DQ02-0101).

Institutional Review Board Statement: Not applicable.

Informed Consent Statement: Not applicable.

Data Availability Statement: Data supporting the results can be found in the manuscript text, tables, and figures.

Conflicts of Interest: The authors declare no conflict of interest.

References

1. Zou, C.; Yang, Z.; Dong, D.; Zhao, Q.; Chen, Z.; Feng, Y.; Li, J.; Wang, X. Formation, distribution and prospect of unconventional hydrocarbons in source rock strata in China. *Earth Sci.* **2022**, *47*, 1517–1533, (In Chinese with English abstract).
2. Loucks, R.G.; Reed, R.M.; Ruppel, S.C.; Jarvie, D.M. Morphology, genesis, and distribution of nanometer-scale pores in siliceous mudstones of the Mississippian Barnett Shale. *J. Sediment. Res.* **2009**, *79*, 848–861. [CrossRef]
3. Katz, B.J.; Arango, I. Organic porosity: A geochemist's view of the current state of understanding. *Org. Geochem.* **2018**, *123*, 1–16. [CrossRef]
4. Wasaki, A.; Akkutlu, I.Y. Permeability of organic-rich shale. *SPE J.* **2015**, *20*, 1384–1396. [CrossRef]
5. Guo, X.; Li, Y.; Borjigen, T.; Wang, Q.; Yuan, T.; Shen, B.; Ma, Z.; Wei, F. Hydrocarbon generation and storage mechanisms of deep-water shelf shales of Ordovician Wufeng Formation–Silurian Longmaxi Formation in Sichuan Basin, China. *Pet. Explor. Dev.* **2020**, *47*, 193–201, (In Chinese with English abstract). [CrossRef]
6. Zou, C.; Dong, D.; Wang, S.; Li, J.; Li, X.; Wang, Y.; Li, D.; Cheng, K. Geological characteristics, formation mechanism and resource potential of shale gas in China. *Pet. Explor. Dev.* **2010**, *37*, 641–653, (In Chinese with English abstract). [CrossRef]
7. Zhao, W.; Bian, C.; Li, Y.; Liu, W.; Dong, J.; Wang, K.; Zeng, X. Organic matter transformation ratio, hydrocarbon expulsion efficiency and shale oil enrichment type in Chang 73 shale of Upper Triassic Yanchang Formation in Ordos Basin, NW China. *Pet. Explor. Dev.* **2023**, *50*, 12–23, (In Chinese with English abstract). [CrossRef]
8. Hill, R.J.; Zhang, E.; Katz, B.J.; Tang, Y. Modeling of gas generation from the Barnett shale, Fort Worth Basin, Texas. *AAPG Bull.* **2007**, *91*, 501–521. [CrossRef]
9. Ko, L.T.; Loucks, R.G.; Zhang, T.; Ruppel, S.C.; Shao, D. Pore and pore network evolution of Upper Cretaceous Boquillas (Eagle Ford-equivalent) mudrocks: Results from gold tube pyrolysis experiments. *AAPG Bull.* **2016**, *100*, 1693–1722. [CrossRef]
10. Borjigin, T.; Tao, C.; Hu, G.; Shen, B.; Ma, Z.; Pan, A.; Wang, J.; Wang, X.; Xu, E. Effect of hydrocarbon explusion efficiency on shale gas formation and enrichment. *Pet. Geol. Exp.* **2020**, *42*, 325–334+344, (In Chinese with English abstract).
11. Jarvie, D.M.; Hill, R.J.; Ruble, T.E.; Pollastro, R.M. Unconventional shale-gas systems: The Mississippian Barnett Shale of north-central Texas as one model for thermogenic shale-gas assessment. *AAPG Bull.* **2007**, *91*, 475–499. [CrossRef]
12. Ko, L.T.; Loucks, R.G.; Ruppel, S.C.; Zhang, T.; Peng, S. Origin and characterization of Eagle Ford pore networks in the South Texas Upper Cretaceous shelf. *AAPG Bull.* **2017**, *101*, 387–418. [CrossRef]
13. Meng, M.; Peng, J.; Ge, H.; Ji, W.; Li, X.; Wang, Q. Rock fabric of lacustrine shale and its influence on residual oil distribution in the Upper Cretaceous Qingshankou Formation, Songliao Basin. *Energy Fuels* **2023**, *37*, 7151–7160. [CrossRef]
14. Peng, J.; Milliken, K.L.; Fu, Q. Quartz types in the Upper Pennsylvanian organic-rich Cline Shale (Wolfcamp D), Midland Basin, Texas: Implications for silica diagenesis, porosity evolution and rock mechanical properties. *Sedimentology* **2020**, *67*, 2040–2064. [CrossRef]

15. Milliken, K.L.; Olson, T. Silica diagenesis, porosity evolution, and mechanical behavior in siliceous mudstones, Mowry Shale (Cretaceous), Rocky Mountains, USA. *J. Sediment. Res.* **2017**, *87*, 366–387. [CrossRef]
16. Milliken, K. Compactional and mass-balance constraints inferred from the volume of quartz cementation in mudrocks. In *Mudstone Diagenesis; Research Perspectives for Shale Hydrocarbon Reservoirs, Seals, and Source Rocks*; Camp, W.K., Milliken, K.L., Taylor, K., Fishman, N., Hackley, P.C., Macquaker, J.H.S., Eds.; American Association of Petroleum Geologists: Tulsa, OK, USA, 2019; Volume 120, pp. 33–48.
17. Dong, T.; He, Q.; He, S.; Zhai, G.; Zhang, Y.; Wei, S.; Wei, C.; Hou, Y.; Guo, X. Quartz types, origins and organic matter-hosted pore systems in the lower cambrian Niutitang Formation, middle yangtze platform, China. *Mar. Petrol. Geol.* **2021**, *123*, 104739. [CrossRef]
18. Milliken, K.L.; Ergene, S.M.; Ozkan, A. Quartz types, authigenic and detrital, in the Upper Cretaceous Eagle Ford Formation, South Texas, USA. *Sediment. Geol.* **2016**, *339*, 273–288. [CrossRef]
19. Niu, X.; Yan, D.; Zhuang, X.; Liu, Z.; Li, B.; Wei, X.; Xu, H.; Li, D. Origin of quartz in the lower Cambrian Niutitang Formation in south Hubei Province, upper Yangtze platform. *Mar. Petrol. Geol.* **2018**, *96*, 271–287. [CrossRef]
20. Xu, H.; Zhou, W.; Hu, Q.; Yi, T.; Ke, J.; Zhao, A.; Lei, Z.; Yu, Y. Quartz types, silica sources and their implications for porosity evolution and rock mechanics in the Paleozoic Longmaxi Formation shale, Sichuan Basin. *Mar. Petrol. Geol.* **2021**, *128*, 105036. [CrossRef]
21. Liu, Z.; Xu, L.; Wen, Y.; Zhang, Y.; Luo, F.; Duan, K.; Chen, W.; Zhou, X.; Wen, J. Accumulation characteristics and comprehensive evaluation of shale gas in Cambrian Niutitang Formation, Hubei. *Earth Sci.* **2022**, *47*, 1586–1603, (In Chinese with English abstract).
22. Chen, X.; Chen, L.; Jiang, S.; Liu, A.; Luo, S.; Li, H.; Li, P.; Chen, P. Evaluation of shale reservoir quality by geophysical logging for Shuijingtuo Formation of Lower Cambrian in Yichang area, central Yangtze. *J. Earth Sci.* **2021**, *32*, 766–777. [CrossRef]
23. Wang, Y.; Zhai, G.; Liu, G.; Shi, W.; Lu, Y.; Li, J.; Zhang, Y. Geological characteristics of shale gas in different strata of marine facies in South China. *J. Earth Sci.* **2021**, *32*, 725–741. [CrossRef]
24. Gao, J.; Li, Y.; He, S.; He, Z.; Li, S.; Wo, Y.; Li, W.; Zhai, G.; Zhao, J. Exploration discovery of shale gas and its indicative significance to mineralization of MVT Lead-Zinc deposit in Yichang area, West Hubei. *Earth Sci.* **2021**, *46*, 2230–2245, (In Chinese with English abstract).
25. Zhai, G.; Wang, Y.; Bao, S.; Guo, T.; Zhou, Z.; Chen, X.; Wang, J. Major factors controlling the accumulation and high productivity of marine shale gas and prospect forecast in Southern China. *Earth Sci.* **2017**, *42*, 1057–1068, (In Chinese with English abstract).
26. Liu, Y.; Zhai, G.; Xu, X.; Zhang, X.; Bai, L.; Yang, Y.; Cao, S. Logging identification of high quality shale of Niutitang Formation and Doushantuo Formation in western Hubei. *Earth Sci.* **2022**, *47*, 1791–1804, (In Chinese with English abstract).
27. Wei, S.; He, S.; Hu, M.; Yang, W.; Guo, X.; Iglauer, S.; Zhai, G. Supercritical high-pressure methane adsorption on the Lower Cambrian Shuijingtuo shale in the Huangling anticline area, South China: Adsorption behavior, storage characteristics, and geological Implications. *Energy Fuels* **2021**, *35*, 19973–19985. [CrossRef]
28. Wei, S.; He, S.; Pan, Z.; Zhai, G.; Yang, R.; Dong, T.; Yang, W. Characteristics and evolution of pyrobitumen-hosted pores of the overmature Lower Cambrian Shuijingtuo Shale in the south of Huangling anticline, Yichang area, China: Evidence from FE-SEM petrography. *Mar. Petrol. Geol.* **2020**, *116*, 104303. [CrossRef]
29. Milliken, K.L. SEM-Based Cathodoluminescence Imaging for Discriminating Quartz Types in Mudrocks. In Proceedings of the SPE/AAPG/SEG Unconventional Resources Technology Conference, Denver, CO, USA, 12–14 August 2013.
30. Xie, X.; Zhu, G.; Wang, Y. The influence of syngenetic hydrothermal silica fluid on organic matter preservation in lower Cambrian Niutitang Formation, South China. *Mar. Petrol. Geol.* **2021**, *129*, 105098. [CrossRef]
31. Gao, P.; He, Z.; Lash, G.G.; Zhou, Q.; Xiao, X. Controls on silica enrichment of lower cambrian organic-rich shale deposits. *Mar. Petrol. Geol.* **2021**, *130*, 105126. [CrossRef]
32. Worden, R.H.; Morad, S. (Eds.) Quartz Cementation in Oil Field Sandstones: A Review of the Key Controversies. In *Quartz Cementation in Sandstones*; Blackwell Science: Oxford, UK, 2000; pp. 1–20.
33. Rutman, P.; Hoareau, G.; Kluska, J.-M.; Lejay, A.; Fialips, C.; Gelin, F.; Aubourg, C.; Bilbao, E.H. Diagenesis and alteration of subsurface volcanic ash beds of the Vaca Muerta Formation, Argentina. *Mar. Petrol. Geol.* **2021**, *132*, 105220. [CrossRef]
34. Zhao, J.; Jin, Z.; Jin, Z.; Wen, X.; Geng, Y. Origin of authigenic quartz in organic-rich shales of the Wufeng and Longmaxi Formations in the Sichuan Basin, South China: Implications for pore evolution. *J. Nat. Gas. Sci. Eng.* **2017**, *38*, 21–38. [CrossRef]
35. Iijima, A.; Tada, R. Silica diagenesis of Neogene diatomaceous and volcaniclastic sediments in northern Japan. *Sedimentology* **1981**, *28*, 185–200. [CrossRef]
36. Halbach, M.; Halbach, P.; Lüders, V. Sulfide-impregnated and pure silica precipitates of hydrothermal origin from the Central Indian Ocean. *Chem. Geol.* **2002**, *182*, 357–375. [CrossRef]
37. Adachi, M.; Yamamoto, K.; Sugisaki, R. Hydrothermal chert and associated siliceous rocks from the northern Pacific their geological significance as indication of ocean ridge activity. *Sediment. Geol.* **1986**, *47*, 125–148. [CrossRef]
38. Yamamoto, K. Geochemical characteristics and depositional environments of cherts and associated rocks in the Franciscan and Shimanto Terranes. *Sediment. Geol.* **1987**, *52*, 65–108. [CrossRef]
39. Boström, K.; Peterson, M.N.A. The origin of aluminum-poor ferromanganoan sediments in areas of high heat flow on the East Pacific Rise. *Mar. Geol.* **1969**, *7*, 427–447. [CrossRef]

40. Hower, J.; Eslinger, E.V.; Hower, M.E.; Perry, E.A. Mechanism of burial metamorphism of argillaceous sediment: 1. Mineralogical and chemical evidence. *GSA Bull.* **1976**, *87*, 725–737. [CrossRef]
41. Peltonen, C.; Marcussen, Ø.; Bjørlykke, K.; Jahren, J. Clay mineral diagenesis and quartz cementation in mudstones: The effects of smectite to illite reaction on rock properties. *Mar. Petrol. Geol.* **2009**, *26*, 887–898. [CrossRef]
42. Bjørlykke, K.; Egeberg, P.K. Quartz cementation in sedimentary basins. *AAPG Bull.* **1993**, *77*, 1538–1548.
43. Isaacs, C.M. Influence of rock composition on kinetics of silica phase changes in the Monterey Formation, Santa Barbara area, California. *Geology* **1982**, *10*, 304–308. [CrossRef]
44. Blood, R.; Lash, G.; Bridges, L. Biogenic silica in the Devonian shale succession of the Appalachian Basin, USA. In Proceedings of the AAPG 2013 Annual Convention and Exhibition, Pittsburgh, PA, USA, 19–22 May 2013; Volume 50864, pp. 19–22.
45. Wright, A.M.; Spain, D.; Ratcliffe, T.K. Application of inorganic whole rock geochemistry to shale resource plays. In Proceedings of the Canadian Unconventional Resources and International Petroleum Conference, Calgary, AB, Canada, 19–21 October 2010.
46. Dong, T.; Harris, N.B.; Ayranci, K.; Yang, S. The impact of rock composition on geomechanical properties of a shale formation: Middle and Upper Devonian Horn River Group shale, Northeast British Columbia, Canada. *AAPG Bull.* **2017**, *101*, 177–204. [CrossRef]
47. Dowey, P.J.; Taylor, K.G. Extensive authigenic quartz overgrowths in the gas-bearing Haynesville-Bossier Shale, USA. *Sediment. Geol.* **2017**, *356*, 15–25. [CrossRef]
48. Sholkovitz, E.R.; Price, N.B. The major-element chemistry of suspended matter in the Amazon Estuary. *Geochim. Cosmochim. Acta* **1980**, *44*, 163–171. [CrossRef]
49. Ross, D.J.K.; Bustin, R.M. Sediment geochemistry of the Lower Jurassic Gordondale Member, northeastern British Columbia. *Bull. Can. Petrol. Geol.* **2006**, *54*, 337–365. [CrossRef]
50. Ross, D.J.K.; Bustin, R.M. Characterizing the shale gas resource potential of Devonian-Mississippian strata in the Western Canada sedimentary basin: Application of an integrated formation evaluation. *AAPG Bull.* **2008**, *92*, 87–125. [CrossRef]
51. Dong, T.; He, S.; Chen, M.; Hou, Y.; Guo, X.; Wei, C.; Han, Y.; Yang, R. Quartz types and origins in the paleozoic Wufeng-Longmaxi Formations, Eastern Sichuan Basin, China: Implications for porosity preservation in shale reservoirs. *Mar. Petrol. Geol.* **2019**, *106*, 62–73. [CrossRef]
52. Zhang, K.; Jiang, Z.; Yin, L.; Gao, Z.; Wang, P.; Song, Y.; Jia, C.; Liu, W.; Liu, T.; Xie, X.; et al. Controlling functions of hydrothermal activity to shale gas content-taking lower Cambrian in Xiuwu Basin as an example. *Mar. Petrol. Geol.* **2017**, *85*, 177–193. [CrossRef]
53. Wedepohl, K.H. Environmental influences on the chemical composition of shales and clays. *Phys. Chem. Earth* **1971**, *8*, 307–333. [CrossRef]
54. Emmings, J.F.; Dowey, P.J.; Taylor, K.G.; Davies, S.J.; Vane, C.H.; Moss-Hayes, V.; Rushton, J.C. Origin and implications of early diagenetic quartz in the Mississippian Bowland Shale Formation, Craven Basin, UK. *Mar. Petrol. Geol.* **2020**, *120*, 104567. [CrossRef]
55. Qiu, Z.; Liu, B.; Dong, D.Z.; Lu, B.; Yawar, Z.; Chen, Z.H.; Schieber, J. Silica diagenesis in the Lower Paleozoic Wufeng and Longmaxi Formations in the Sichuan Basin, South China: Implications for reservoir properties and paleoproductivity. *Mar. Petrol. Geol.* **2020**, *121*, 104594. [CrossRef]
56. Van der Weijden, C.H. Pitfalls of normalization of marine geochemical data using a common divisor. *Mar. Geol.* **2002**, *184*, 167–187. [CrossRef]
57. Tribovillard, N.; Algeo, T.J.; Lyons, T.; Riboulleau, A. Trace metals as paleoredox and paleoproductivity proxies: An update. *Chem. Geol.* **2006**, *232*, 12–32. [CrossRef]
58. Perry, E.; Hower, J. Burial diagenesis in Gulf Coast Pelitic sediments. *Clays Clay Miner.* **1970**, *18*, 165–177. [CrossRef]
59. Hoffman, J.; Hower, J. Clay mineral assemblages as low grade metamorphic geothermometers: Application to the thrust faulted disturbed belt of Montana, USA. In *Aspects of Diagenesis*; Scholle, P.A., Schluger, P.R., Eds.; SEPM Society for Sedimentary Geology: Tulsa, OK, USA, 1997; pp. 55–79.
60. Bjørlykke, K. Clay mineral diagenesis in sedimentary basins—A key to the prediction of rock properties. Examples from the North Sea Basin. *Clay Miner.* **1998**, *33*, 15–34. [CrossRef]
61. Mondol, N.H.; Bjørlykke, K.; Jahren, J.; Høeg, K. Experimental mechanical compaction of clay mineral aggregates—Changes in physical properties of mudstones during burial. *Mar. Petrol. Geol.* **2007**, *24*, 289–311. [CrossRef]
62. Thyberg, B.; Jahren, J. Quartz cementation in mudstones: Sheet-like quartz cement from clay mineral reactions during burial. *Pet. Geosci.* **2011**, *17*, 53–63. [CrossRef]
63. Metwally, Y.M.; Chesnokov, E.M. Clay mineral transformation as a major source for authigenic quartz in hermos-mature gas shale. *Appl. Clay Sci.* **2012**, *55*, 138–150. [CrossRef]
64. Van de Kamp, P.C. Smectite-illite-muscovite transformations, quartz dissolution, and silica release in shales. *Clays Clay Miner.* **2008**, *56*, 66–81. [CrossRef]
65. Środoń, J.; Zeelmaekers, E.; Derkowski, A. The charge of component layers of illite-smectite in bentonites and the nature of end-member illite. *Clays Clay Miner.* **2009**, *57*, 649–671. [CrossRef]
66. Fu, H.; Yan, D.; Yao, C.; Su, X.; Wang, X.; Wang, H.; Li, Y. Pore structure and multi-scale fractal characteristics of adsorbed pores in marine shale: A case study of the Lower Silurian Longmaxi shale in the Sichuan Basin, China. *J. Earth Sci.* **2022**, *33*, 1278–1290. [CrossRef]

67. Meng, M.; Ge, H.; Shen, Y.; Ji, W.; Li, Z. Insight into water occurrence and pore size distribution by nuclear magnetic resonance in marine shale reservoirs, southern China. *Energy Fuels* **2023**, *37*, 319–327. [CrossRef]
68. Fishman, N.S.; Egenhoff, S.O.; Boehlke, A.R.; Lowers, H.A. Petrology and diagenetic history of the upper shale member of the late Devonian-early Mississippian Bakken Formation, Williston Basin, North Dakota. In *Special Paper of the Geological Society of America*; Geological Society of America: Boulder, CO, USA, 2015; Volume 515, pp. 125–151.
69. Han, Y.; Horsfield, B.; Wirth, R.; Mahlstedt, N.; Bernard, S. Oil retention and porosity evolution in organic rich shales. *AAPG Bull.* **2017**, *101*, 807–827. [CrossRef]
70. Bernard, S.; Wirth, R.; Schreiber, A.; Schulz, H.-M.; Horsfield, B. Formation of nanoporous pyrobitumen residues during maturation of the Barnett Shale (Fort Worth Basin). *Int. J. Coal Geol.* **2012**, *103*, 3–11. [CrossRef]
71. Curtis, M.E.; Cardott, B.J.; Sondergeld, C.H.; Rai, C.S. Development of organic porosity in the Woodford Shale with increasing thermal maturity. *Int. J. Coal Geol.* **2012**, *103*, 26–31. [CrossRef]
72. Yang, W.; He, S.; Zhai, G.; Tao, Z.; Yuan, X.; Wei, S. Maturity assessment of the Lower Cambrian and Sinian shales using multiple technical approaches. *J. Earth Sci.* **2021**, *32*, 1262–1277. [CrossRef]
73. Mastalerz, M.; Drobniak, A.; Stankiewicz, A.B. Origin, properties, and implications of solid bitumen in source-rock reservoirs: A review. *Int. J. Coal Geol.* **2018**, *195*, 14–36. [CrossRef]
74. Milliken, K.L.; Zhang, T.; Chen, J.; Ni, Y. Mineral diagenetic control of expulsion efficiency in organic-rich mudrocks, Bakken Formation (Devonian-Mississippian), Williston Basin, North Dakota, U.S.A. *Mar. Petrol. Geol.* **2021**, *127*, 104869. [CrossRef]